Volume 1 | Number 1 | Jan 2013 | Pages 1–100

Nanoscale

www.rsc.org/nanoscale

ROYAL SOCIETY OF CHEMISTRY

ROYAL SOCIETY OF CHEMISTRY

www.rsc.org/nanoscale

Journal Name

ARTICLE TYPE

Structure dependent active sites of Ni_xS_y as an electrocatalyst for hydrogen evolution reaction

Dong Young Chung [a,b,‡]**, Joung Woo Han** [c, ‡]**, Dong-Hee Lim** [d]**, Jun-Ho Jo** [e]**, Sung Jong Yoo** [e***]**, Hyunjoo Lee** [f**] **and Yung-Eun Sung** [a,b*]

Structure effect of NiS and Ni_3S_2 nanoparticles were investigated for their electrocatalytic activity in the hydrogen evolution reaction in both acid and alkaline media. Owing to the different atomic configurations and crystalline structures, there is a hydrogen adsorption energy difference, which induces a difference in
10 the activity. From density functional theory calculations and experimental observation, the importance of designing an electrocatalyst with an appropriate atomic configuration is evident.

Introduction

Hydrogen generation is a key issue to achieving hydrogen economy. [1, 2] Pt group metal is the state of the art hydrogen
15 evolution reaction (HER) electrocatalyst. [3, 4] Because of its limited abundance and high cost, many researchers have focused on developing less expensive and more stable catalysts for HER. Metal sulfides such as MoS_2 and WS_2 are good alternatives for Pt. [5, 6] Many researchers have struggled to find and expose the active
20 sites. However, the exact mechanism and general explanation have not been clearly elucidated yet. Recently computational methods such as density functional theory (DFT) calculation have been conducted to discover materials with high HER activity. [7, 8] In particular, engineering of the edge sites compared to the basal
25 plane can enhance the activity. [9, 10] Other candidates for HER catalysis are nickel alloy materials. [11-14] Recently, nickel phosphide and nickel disulfide catalyst for HER have been reported. [15, 16] Their high activity broadens the possibilities of Ni-based catalysts for HER. Amorphous nickel sulfide as an HER
30 electrocatalyst was also reported previously. [17, 18] However crystalline nickel sulfide has not yet been reported except NiS_2 which has a metal dichalcogenide structure. [16] Structure dependent activity is fundamentally important for a variety of electrochemical reactions such as oxygen reduction reaction
35 (ORR), oxygen evolution reaction (OER) and HER. Many researchers have studied structure-dependent electrochemical activity. Su *et al.* reported the phase-dependent activity of manganese oxide for ORR and OER. [19] Norskov's group reported the structure-dependent OER activity of cobalt oxide. [20] Ni_2P
40 (001) has also been identified as a potential catalyst for HER, as verified by theory and experiment. [15] To utilize nickel sulfide materials for electrochemical applications, a detailed understanding of the structure dependence of nickel sulfide should is required.
45 In this work, we successfully synthesized nickel sulfide

nanoparticle with well-developed exposed facet. By applying NiS and Ni_3S_2 nanoparticles to the HER, we confirmed their different activities. The different structures and atomic configuration result in different hydrogen adsorption energies, which affect the
50 activity, as shown by DFT analysis and experiment. We expect that this structure dependent activity is critical for designing new catalysts for electrochemical systems.

Experimental

Synthesis of the NiS nanoparticles

55 The synthesis of NiS and Ni_3S_2 were adopted from previous reports. [21, 22] Nickel acetylacetonate (Ni(acac)$_2$, Aldrich, 95 %) 385 mg, 1-dodecanethiol (Aldrich, 90 %) 2 ml and oleylamine (Aldrich, 90%) 10 ml were put into a three-necked flask. The flask was heated to 280 °C and maintained there for 5 h with
60 stirring and refluxing under N_2 atmosphere. After the reaction, the flask was cooled to room temperature. The solution was then washed with hexane several times. The washed NiS nanoparticles were dispersed in ethanol.

Synthesis of the Ni_3S_2 nanoparticles

65 Nickel acetylacetonate (Ni(acac)$_2$, Aldrich, 95 %) 200 mg, cysteamine (Aldrich, 95%) 50 mg and 1,5-pentanediol (Aldrich, 96 %) 20 ml were put into a three-necked flask. The flask was heated to 250 °C and maintained for 30 min while stirring and refluxing under a N_2 atmosphere. After the reaction, the flask was
70 cooled to room temperature. The solution was then washed with isopropanol several times. The washed Ni_3S_2 nanoparticles were dispersed in ethanol.

Physical characterization

The high-resolution TEM (HR-TEM) was performed on an
75 analytical TEM Technai F20, operated at 200 kV. Line scanning and elemental composition data were obtained by Philips tecnai
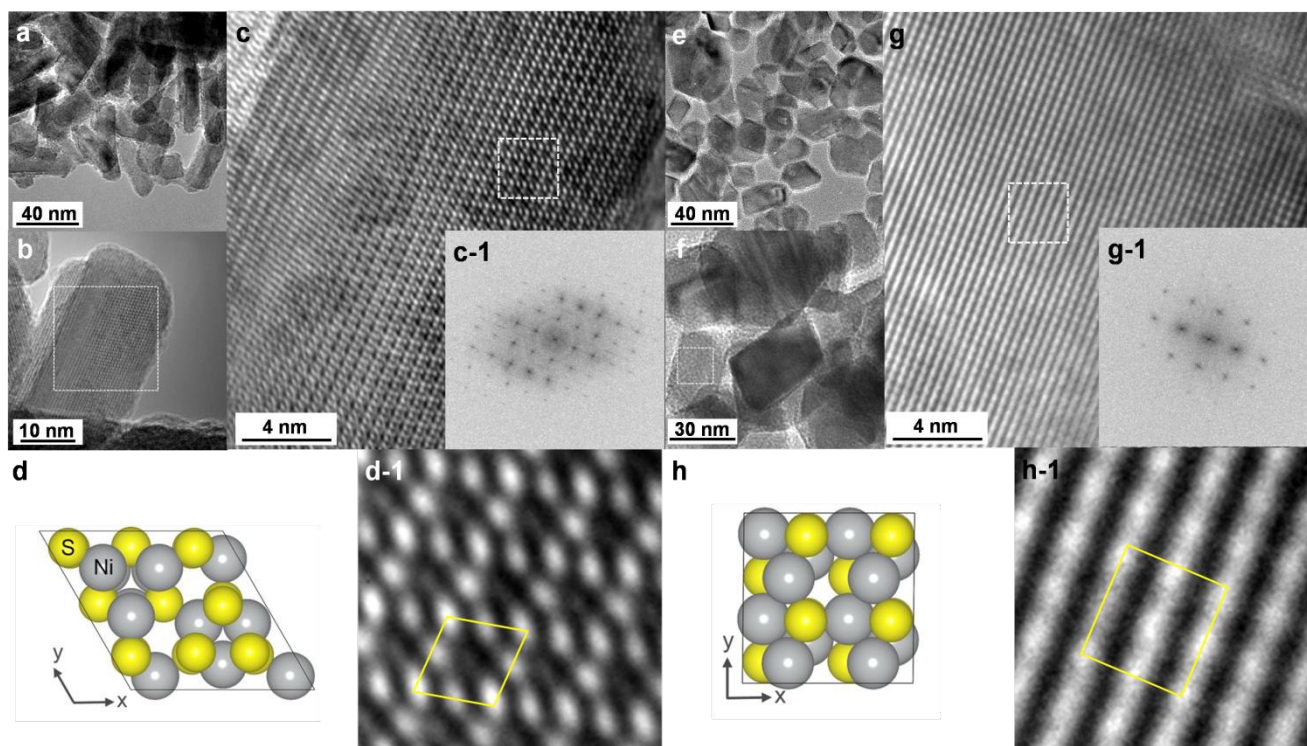
Fig. 1 HR-TEM images of (a-d) NiS nanoparticles and (e-h) Ni₃S₂ nanoparticles. .(Fig 1c and Fig 1g are magnified images from Fig 1b and Fig 1f white region, respectively; (c-1, g-1) power spectrum of the whole images in Fig. 1c and Fig. 1g, respectively.) (d,h) model structure of each basis and (d-1, h-1) magnified images of white square marked region of Fig. 1c and Fig. 1g, respectively.

TF30 ST operated at 300 kV. X-ray diffraction (XRD) patterns were obtained with a Rigaku Miniflex diffactometer (Cu Kα source, λ=1.541 Å). The 2θ angular regions between 15 ° and 80 ° were explored at a scan rate of 2 °min⁻¹ with the angular resolution of 0.02 °. Ni K-edge X-ray absorption spectroscopy was carried out using the beamline 8C Nanoprobe XAFS at the Pohang Accelerator Laboratory (PAL).

Electrochemical measurement

The prepared samples (5 mg) were mixed with Nafion (15 wt%) as a binder and dissolved in the 2-propanol. 7 μL of solutions were deposited on a glassy carbon electrode. Electrochemical measurements were conducted using an Autolab potentiostat (PGSTAT) in a standard three-electrode cell with Pt counter electrode and saturated calomel electrode for reference electrode. All the potentials were represented as a reversible hydrogen electrode (RHE) with an H_2 oxidation calibration method. The HER was measured under 0.5 M H_2SO_4 electrolyte at 293 K (acid condition) and under 0.1 M KOH electrolyte (alkaline condition). Electrochemical double layer capacitance was measured under 0.5 M H_2SO_4 electrolyte. The potential range was selected without faradic reaction. The cyclic voltammograms (CV) was measured with different scan rate. The reference Pt/C was used 20 wt.% (Johnson Matthey)

Computational Methodology

Spin-polarized density functional theory calculations were performed using the Vienna ab initio Simulation Package (VASP) [23-26] with the projector-augmented wave (PAW) [27, 28] method.

Electron exchange-correlation functionals were represented with the generalized gradient approximation (GGA), and the model of Perdew, Burke and Ernzerhof (PBE) [29] was used for the nonlocal corrections. A kinetic energy cutoff of 300 eV was used with a plane-wave basis set. Bulk structures of NiS and Ni₃S₂ were obtained from experimental data of Rajamani and Rrewitt [30] and Parise [31], respectively. The space groups and DFT optimized lattice parameters of bulk NiS and Ni₃S₂ are R3m (a=9.596 Å, b=9.596 Å, c=3.137 Å, α=90°, β=90°, γ=120°) and R32 (a=4.078 Å, b=4.078 Å, c=4.078 Å, α=89.5°, β=89.5°, γ=89.5°), respectively. Errors associated with the DFT calculated lattice parameters compared to the experimental data are less than 0.4 and 0.2% for NiS and Ni₃S₂, respectively. A rhombus-shaped supercell (9.60 × 9.60 × 18.82 Å) with a vacuum space of 9.8 Å and a tetragonal supercell (8.16 × 8.16 × 24.47 Å) with a vacuum space of 14.4 Å were used for the NiS and Ni₃S₂ surfaces, respectively. The Brillouin zone integration of the NiS−(1×1) and Ni₃S₂−(2×2) surfaces were carried out using 6 × 6 × 1 and 4 × 4 × 1 Monkhorst-Pack grid[32], respectively, and first-order Methfessel-Paxton smearing[33] with a width of 0.1 eV. All atoms were fully relaxed and optimized until the total energy change upon two steps of the electronic self-consistent loop was less than 10⁻⁴ eV.

Results and discussion

Fig. 1 shows the high resolution transmission electron microscopy (HR-TEM) images demonstrating that the synthesis of NiS and Ni₃S₂ nanoparticles was well conducted. Most of the
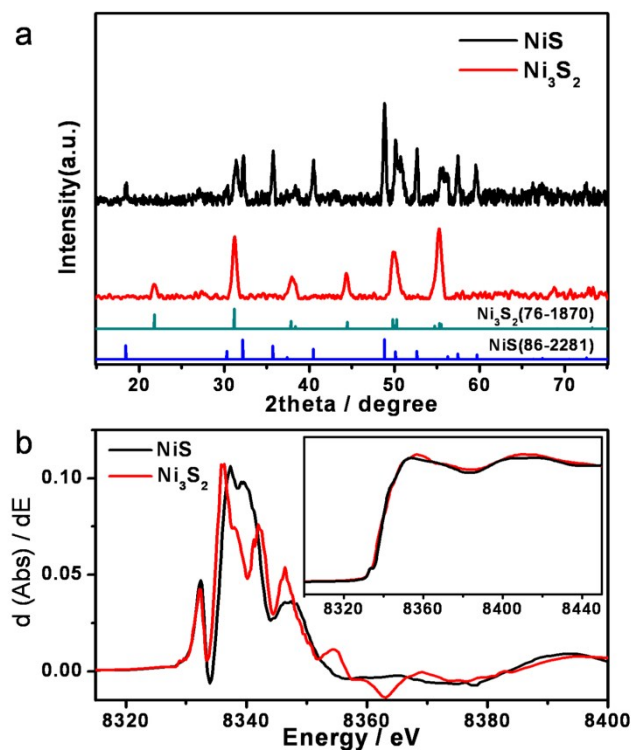
Fig. 2 Characterization of the physical structure. (a) XRD patterns of the sample, (b) derivatives of the Ni K edge X-ray absorption spectra results. (The inset shows the XANES spectra.)

5 NiS nanoparticles were rod shaped, as revealed by close inspection of the HR-TEM images (Fig. 1a). However, the shape of the Ni_3S_2 is octahedral. From the high resolution images and their power spectrum patterns, both nanoparticles were highly 10 single crystalline structure. In particular, the magnified HR-TEM images (Fig. 1d-1 and h-1) are directly matched with the NiS and Ni_3S_2 basis structures, as shown in Fig. 1d and h, respectively. The average size of the NiS nanoparticles was 20 nm wide and 50 nm long, and that of the Ni_3S_2 nanoparticles was around 40 nm.

15 Fig. 2a shows the powder X-ray diffraction (XRD) patterns, confirming the formation of nanoparticles. The XRD pattern of the NiS nanoparticles matched with the PDF number (86-2281) and that of Ni_3S_2 was also well-matched with the PDF number (76-1870). To figure out the atomic ratio, we conducted scanning 20 transmission electron microscopy - energy dispersive X-ray spectroscopy (STEM-EDS) analysis of NiS and Ni_3S_2. The line scan and EDS analysis suggest well matched atomic ratio each samples, respectively. (see in supporting information, Fig. S1 and Table. S1) The chemical nature of the local Ni structure in the 25 nanoparticles was investigated by X-ray absorption spectroscopy (XAS) as shown in Fig. 2b. From the pre-edge region XANES spectra, the peak (8333 eV) reflects the electron transition from the Ni 1s orbitals to the 3d orbitals. The intensity is related to the coordination of the Ni^{2+} ion with the sulfur anions. From the edge 30 region, NiS was positively shifted compared to that of Ni_3S_2 which agreed well with the chemical state of Ni of each structure.

The ir-corrected electrocatalytic behavior of the nickel sulfide nanoparticles for the hydrogen evolution reaction (HER) in 0.5 M
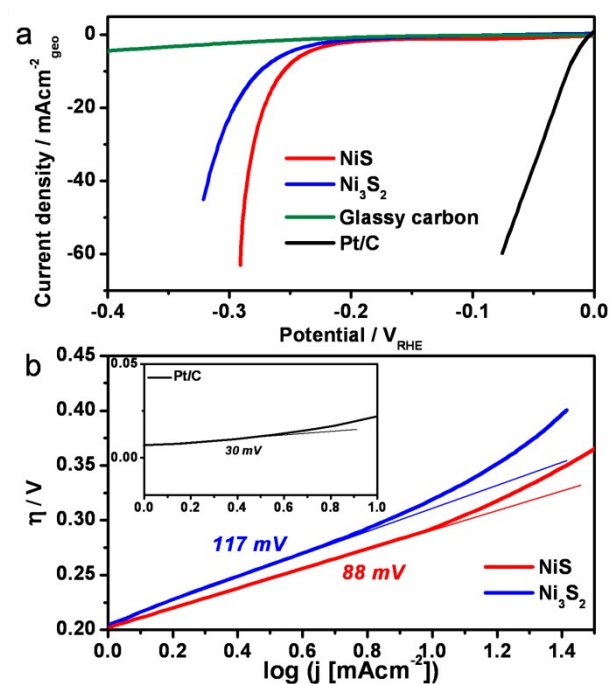
35 **Fig. 3** Electrochemical measurements of the hydrogen evolution reaction. (a) HER activity at 0.5 M H_2SO_4 at a rate of 50 mVs^{-1}. (b) Tafel plot. (inset: Pt/C Tafel plot)

H_2SO_4 is shown in Fig. 3a. The electrocatalytic activities of the 40 nanoparticle samples were measured using glassy carbon electrode. The glassy carbon refers to the results as an electrocatalyst without further loading of catalyst. To compare the activity, 20 wt% Pt/C electrocatalyst was also measured. The activity increases in the order of bare < Ni_3S_2 < NiS. It is 45 intriguing that the activity of NiS is much larger than that of Ni_3S_2. To confirm the activity difference, we performed a Tafel analysis as shown in Fig. 3b. The Tafel plot, which is cross-related to the reaction mechanisms, shows a much smaller Tafel slope for NiS compared to Ni_3S_2. The HER mechanism under 50 acidic media was considered to occur through three possible steps.[3] The first step is the Volmer step which is the primary discharge step.[4]

$$H_3O^+ + e^- \rightarrow H_{ad} + H_2O \quad (Volmer)$$
(subscript ad means adsorbed to the catalyst) (1)

55
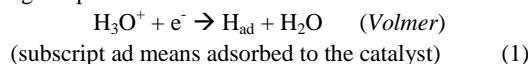
$$b = 2.3RT / \alpha F = 120 \text{ mV}$$
(if, the symmetric factor of α is estimated as 0.5)

After the Volmer step, there are two possible steps. The first one 60 is the Heyrovsky reaction

$$H_{ad} + H_3O^+ + e^- \rightarrow H_2 + H_2O, \, b = 40 \text{ mV} \, (Heyrovsky) \, (2)$$
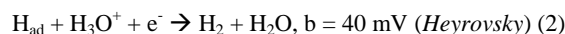
and the second is a Tafel reaction,

65

$$H_{ad} + H_{ad} \rightarrow H_2, \, b = 30 \text{ mV} \, (Tafel) \quad (3)$$
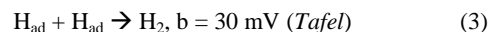
Considering that the Tafel slope of Ni_3S_2 is 117 mVdec^{-1}, the
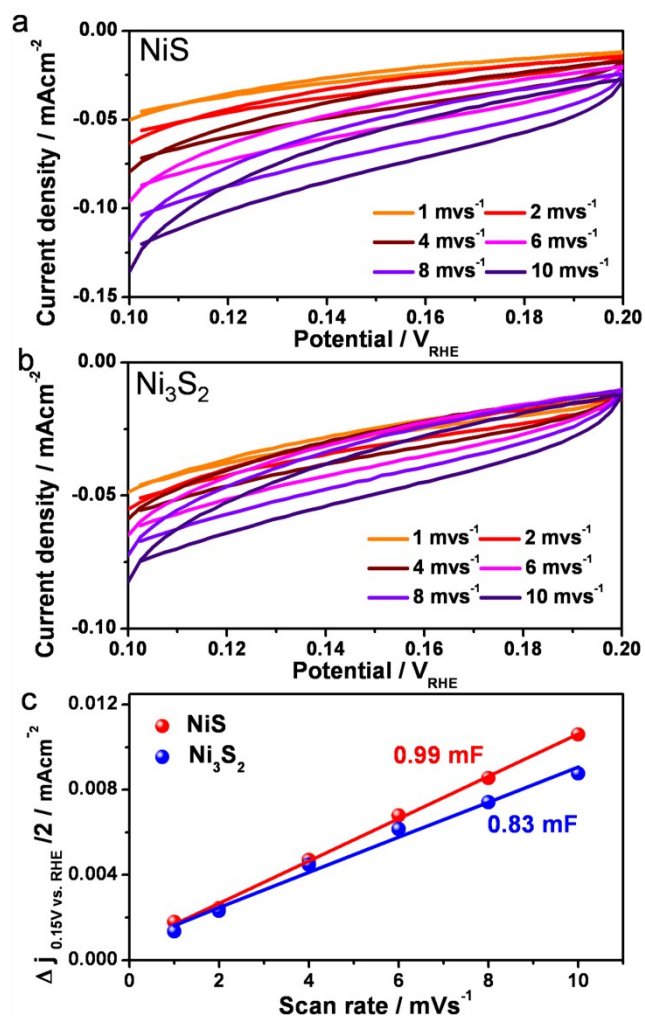
Fig. 4 Electrochemical double layer capacitance analysis (a) cyclic voltammogram (CV) of NiS at different scan rate, (b) that of Ni$_3$S$_2$ (c) linear fitting of capacitive currents of the catalyst vs scan rate.
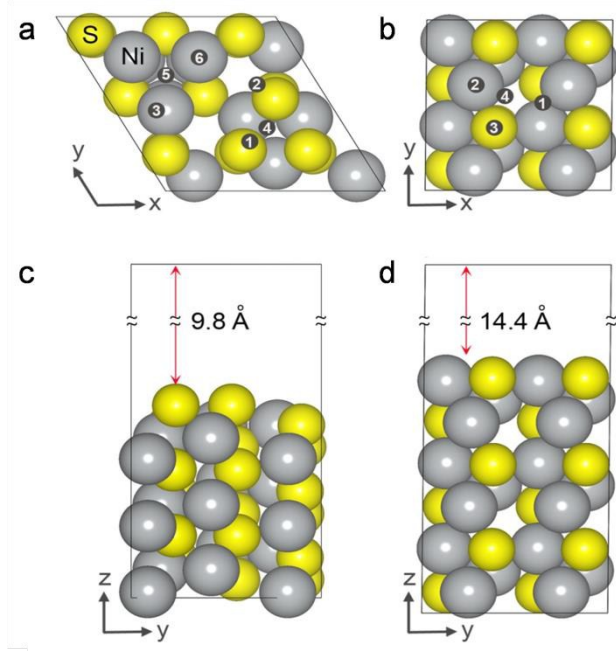
Fig. 5 Crystal structure. Top views of the NiS (a) and Ni$_3$S$_2$ (b) surfaces with the optimized adsorption configurations of atomic hydrogen. Side views of the NiS (c) and Ni$_3$S$_2$ (d) surfaces with vacuum space distances. The large (gray) and small (yellow) spheres represent Ni and S, respectively. Solid lines indicate the supercells.

Table 1. Adsorption energies (eV) of atomic hydrogen on the NiS and Ni$_3$S$_2$ surfaces. The adsorption sites (1–6) are shown in Fig 5.

	Adsorption sites					
	1	2	3	4	5	6
NiS	-4.65	-4.27	-3.99	-3.70	-3.60	-2.97
Ni$_3$S$_2$	-3.13	-2.96	-2.51	-2.22		

rate-determining step is the Volmer step, in which proton adsorption does not occur readily. These results agree well with those of other metal sulfide materials such as MoS$_2$. [34, 35] To estimate and compare the electrochemical active surface area, we conducted the CV method to measure the electrochemical double-layer capacitance (EDLC). [36-38] The potential range was selected without faradic reaction. The CV was measured with different scan rate. (Fig. 4a and b) The halves of the anodic and cathodic current density difference at the center of the potential range are plotted versus the scan rate as shown in Fig. 4c. The EDLC of NiS and Ni$_3$S$_2$ is 0.99 and 0.83 mF, respectively. Concerning the similar EDLC values, the effective surface area is not the critical factor to determine the activity trend. We estimate that the proton adsorption intensity is the factor in predicting the activity. In the case of the NiS nanoparticles, the Tafel slope is much lower than 120 mVdec^{-1}, which is the Volmer step constant. The value is almost intermediate in two steps, which may be attributed to the proton adsorption being much easier than for the Ni$_3$S$_2$. NiS is known as a good co-catalyst with CdS by electron transfer

(proton adsorption) and electrochemical desorption under visible light in acidic conditions. These properties may also mean that NiS has appropriate adsorption intensity. [39]

The electrocatalytic activity for the HER forms a volcano like shape with respect to the hydrogen catalyst adsorption strength.[7] This tendency was correlated to the Sabatier principle, which states that the optimal catalytic activity is obtained by optimizing the strength of the interaction between the adsorbate and catalyst. [40] If hydrogen is too strongly bound to the catalyst, the desorption in the intermediate step should be rate determining[8]. Considering that the Tafel slope of metal sulfide was matched with Volmer step except some cases [6], the weak H adsorption has been considered to be the main rate determining step. In our case, the tafel slope of NiS is 88 and that of Ni$_3$S$_2$ is 117 mVdec^{-1} which showes Volmer step. We considered that higher HER activity of NiS may be originated from rather strong H adsorption energy. From this view, we calculated the
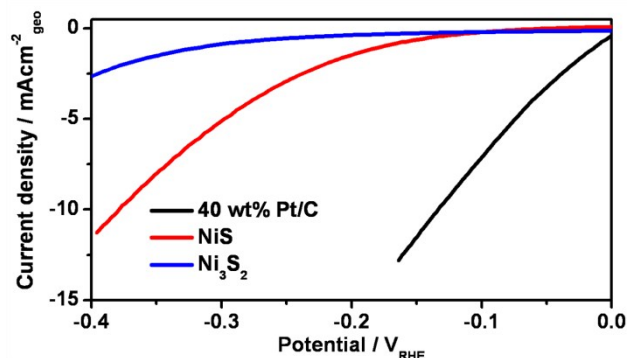
Fig. 6 Electrochemical measurement of the hydrogen evolution reaction in 0.1 M KOH at a scan rate of 50mVs^{-1}.

[5] adsorption intensity using density functional theory (DFT) calculations to explain the high activity of NiS compared to the Ni$_3$S$_2$.

An HER activity study through DFT analysis was conducted to determine out the activity parameter. The simple atomic scale [10] descriptor facilitates and generalizes the mechanism study. Greeley *et al*. suggested that the free energy of the hydrogen adsorption parameter was well correlated to the overall HER activity. [7] To understand the activity enhancement of NiS compared to Ni$_3$S$_2$, which has a similar composition but different [15] structure, we compared the hydrogen adsorption intensity, as many studies have already suggest that the rate-determining step of metal sulfides is related to their weak hydrogen adsorption intensity. [8] We modeled the possible adsorption sites in each case under the correlations of the specific facet determined by the HR-[20] TEM and XRD results. (Fig 1g and h) The adsorption energy (E$_{ads}$) of atomic hydrogen is defined as E$_{ads}$ = E$_{Surf+H}$ − E$_{Surf}$ − E$_H$, where E$_{Surf+H}$, E$_{Surf}$, and E$_H$ are the total energies of the NiS and Ni$_3$S$_2$ systems with adsorbed H, bare NiS and Ni$_3$S$_2$ surfaces, and a single gas phase hydrogen atom.

[25] A negative adsorption energy indicates that the adsorption is exothermic, with the adsorbed hydrogen being more stable than the free gas phase hydrogen. Nine adsorption sites of atomic hydrogen were examined on both the NiS and Ni$_3$S$_2$ surfaces. Among the examined adsorption sites, the optimized stable [30] configurations of adsorbed hydrogen on NiS and Ni$_3$S$_2$ are shown in Fig. 5a and b, respectively. Table 1 summarizes the H adsorption energies. Considering the adsorption energy, the HER activity trends of NiS and Ni$_3$S$_2$ are well correlated. Governed by the Volmer step, in which hydrogen adsorption is the rate-[35] determining step, a strong adsorption energy induced a more facile reaction. The average hydrogen adsorption energy of NiS is 1eV below that of Ni$_3$S$_2$ which explains its higher electrocatalytic activity. From the DFT analysis, we confirmed the HER activity trend and found that the atomic configuration strongly affects the [40] adsorption intensity and activity. By engineering the structure and atomic configuration through strain, we expect further activity enhancements will be possible.

We also conducted HER measurement in alkaline media as shown in Fig. 6. In alkaline media, the HER pathway could be [45] through the Volmer–Heyrovsky process or Volmer–Tafel pathways. [41, 42]
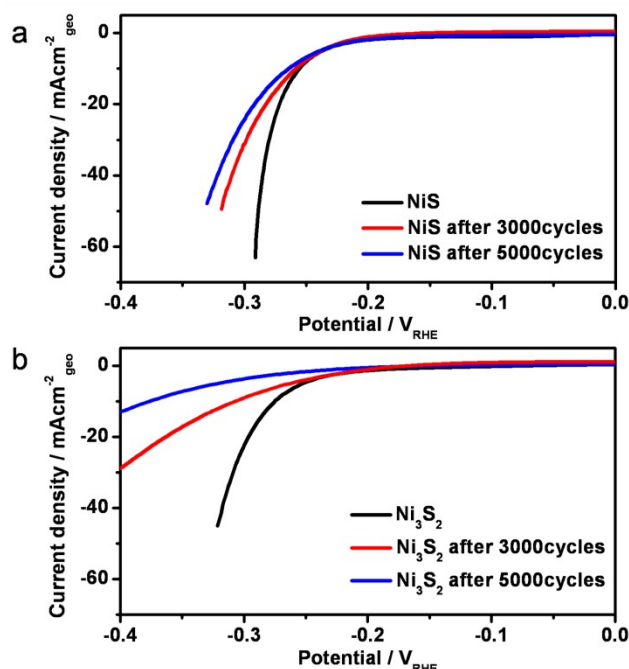
Fig. 7 Long-term durability test to confirm the electrochemical stability (a) NiS and (b) Ni$_3$S$_2$. Long-term durability test was conducted potential [50] cycling from 0 V$_{RHE}$ to -0.3 V$_{RHE}$ at a rate of 50mVs^{-1}.

$$H_2O + e^- \rightarrow H_{ad} + OH^- \ (Volmer)$$
$$\text{and } H_{ad} + H_{ad} \rightarrow H_2 \ (Tafel) \tag{4}$$

[55]
$$H_2O + e^- \rightarrow H_{ad} + OH^- \ (Volmer)$$
$$\text{and } H_2O + H_{ad} + e\text{-} \rightarrow H_2 + OH^- \ (Heyrovsky) \ (5)$$
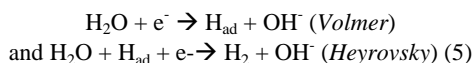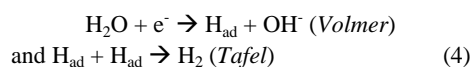
Gong *et al*. suggested synergistic effect of nickel oxide/nickel heterostructures, which OH$^-$ generated by the H$_2$O splitting could [60] preferentially attach the NiO and Ni site could help the H adsorption. [43] Considering that both NiS and Ni$_3$S$_2$ has positively charged Ni state, which has strong OH$^-$ binding energy of, rather strong H atom binding energy can facilitate the Volmer process and thus enhance the overall HER activity.

[65] To utilize the catalyst for the HER, not only high activity but long-term stability should be also considered. [44] Long-term stability test was conducted by continuous CV cycles and the polarization curves were tested after 3000 and 5000 cycles as shown in Fig. 7. The CV was measure through potential cycling [70] from 0 V$_{RHE}$ to -0.3V$_{RHE}$ at a rate of 50 mvs^{-1}. The activity of NiS was little deactivated after 5000 cycles compared to that of Ni$_3$S$_2$. Considering both high long-term stability and activity, NiS can be a good candidate for the HER compared to Ni$_3$S$_2$. However, nano-architecturing [35,45] or hybrid structure with support [75] materials [6,46] to improve the electrochemical and thermodynamic stability and activity should be required utilizing the nickel sulfide materials as real applications to HER reaction

Conclusions

We have synthesized nickel sulfide nanoparticles and

confirmed their electrocatalytic activity for the HER in acidic and alkaline media. Because of its strong affinity for hydrogen, NiS has a higher activity than Ni_3S_2, as shown experimentally and theoretically. In the case of Ni_3S_2, the rate determining step is the Volmer step whereas, that of NiS is the mixed Volmer and Heyrovsky reaction, as is confirmed by Tafel analysis. We expect that controlling the facet or nanoparticle engineering of nickel sulfide can provide good candidates for water electrolysis catalysts.

Acknowledgements

Notes and references

[a] Center for Nanoparticle Research, Institute for Basic Science (IBS), Seoul 151-742, Republic of Korea

[b] School of Chemical and Biological Engineering, Seoul National University, Seoul 151-742, Republic of Korea; E-mail: ysung@snu.ac.kr

[c] Department of Chemical and Biomolecular Engineering, Yonsei University, Seoul 120-749, Republic of Korea

[d] Department of Environmental Engineering, Chungbuk National University, Chungbuk 361-763, Republic of Korea

[e] Fuel Cell Research Center, Korea Institute of Science and Technology, 39-1 Hawolgok-dong, Seoul 136-791, Korea; E-mail: ysj@kist.re.kr

[f] Department of Chemical and Biomolecular Engineering, Korea Advanced Institute of Science and Technology (KAIST), Daejeon, 305-701, Korea; E-mail: azhyun@kaist.ac.kr

† Electronic Supplementary Information (ESI) available: STEM-EDS analysis data. See DOI: 10.1039/b000000x/

‡ These authors are equally contributed.

1. N. S. Lewis and D. G. Nocera, *Proc. Natl. Acad. Sci. U. S. A.*, 2006, **103**, 15729-15735.
2. J. A. Turner, *Science*, 2004, **305**, 972-974.
3. B. E. Conway and B. V. Tilak, *Electrochim. Acta*, 2002, **47**, 3571-3594.
4. W. Sheng, H. A. Gasteiger and Y. Shao-Horn, *J. Electrochem. Soc.*, 2010, **157**, B1529-B1536.
5. D. Merki and X. Hu, *Energy Environ. Sci.*, 2011, **4**, 3878-3888.
6. Y. Li, H. Wang, L. Xie, Y. Liang, G. Hong and H. Dai, *J. Am. Chem. Soc.*, 2011, **133**, 7296-7299.
7. J. Greeley, T. F. Jaramillo, J. Bonde, I. Chorkendorff and J. K. Nørskov, *Nat. Mater.*, 2006, **5**, 909-913.
8. B. Hinnemann, P. G. Moses, J. Bonde, K. P. Jørgensen, J. H. Nielsen, S. Horch, I. Chorkendorff and J. K. Nørskov, *J. Am. Chem. Soc.*, 2005, **127**, 5308-5309.
9. T. F. Jaramillo, K. P. Jørgensen, J. Bonde, J. H. Nielsen, S. Horch and I. Chorkendorff, *Science*, 2007, **317**, 100-102.
10. J. Kibsgaard, Z. Chen, B. N. Reinecke and T. F. Jaramillo, *Nat. Mater.*, 2012, **11**, 963-969.
11. K. Ngamlerdpokin and N. Tantavichet, *Int. J. Hydrogen Energy*, 2014, **39**, 2505-2515.
12. K. A. Kuttiyiel, K. Sasaki, W. F. Chen, D. Su and R. R. Adzic, *J. Mat. Chem. A*, 2014, **2**, 591-594.
13. B. M. Jović, U. Č. Lačnjevac, N. V. Krstajić and V. D. Jović, *Electrochim. Acta*, 2013, **114**, 813-818.
14. S. H. Ahn, H. Y. Park, I. Choi, S. J. Yoo, S. J. Hwang, H. J. Kim, E. Cho, C. W. Yoon, H. Park, H. Son, J. M. Hernandez, S. W. Nam, T. H. Lim, S. K. Kim and J. H. Jang, *Int. J. Hydrogen Energy*, 2013, **38**, 13493-13501.
15. E. J. Popczun, J. R. McKone, C. G. Read, A. J. Biacchi, A. M. Wiltrout, N. S. Lewis and R. E. Schaak, *J. Am. Chem. Soc.*, 2013, **135**, 9267-9270.
16. D. Kong, J. Cha, H. Wang, H. R. Lee and Y. Cui, *Energy Environ. Sci.*, 2013, **6**, 3553-3558.
17. Q. Han, K. Liu, J. Chen and X. Wei, *Int. J. Hydrogen Energy*, 2003, **28**, 1207-1212.
18. I. Paseka, *Electrochim. Acta*, 1993, **38**, 2449-2454.
19. H. Y. Su, Y. Gorlin, I. C. Man, F. Calle-Vallejo, J. K. Norskov, T. F. Jaramillo and J. Rossmeisl, *Phys. Chem. Chem. Phys.*, 2012, **14**, 14010-14022.
20. M. García-Mota, M. Bajdich, V. Viswanathan, A. Vojvodic, A. T. Bell and J. K. Nørskov, *J. Phys. Chem. C*, 2012, **116**, 21077-21082.
21. W. S. Chi, J. W. Han, S. Yang, D. K. Roh, H. Lee and J. H. Kim, *Chem. Commun.*, 2012, **48**, 9501-9503.
22. K. Aso, H. Kitaura, A. Hayashi and M. Tatsumisago, *J. Mater. Chem.*, 2011, **21**, 2987-2990.
23. G. Kresse and J. Hafner, *Phys. Rev. B*, 1993, **47**, 558-561.
24. G. Kresse and J. Hafner, *Phys. Rev. B*, 1994, **49**, 14251-14269.
25. G. Kresse and J. Furthmüller, *Phys. Rev. B*, 1996, **54**, 11169-11186.
26. G. Kresse and J. Furthmüller, *Comput. Mater. Sci.*, 1996, **6**, 15-50.
27. P. E. Blöchl, *Physical Review B*, 1994, **50**, 17953-17979.
28. G. Kresse and D. Joubert, *Physical Review B*, 1999, **59**, 1758-1775.
29. J. P. Perdew, K. Burke and M. Ernzerhof, *Phys. Rev. Lett.*, 1996, **77**, 3865-3868.
30. V. Rajamani and C. T. Prewitt, *The Canadian Mineralogist*, 1974, **12**, 253-257.
31. J. B. Parise, *Acta Crystallogr. Sec. B*, 1980, **36**, 1179-1180.
32. H. J. Monkhorst and J. D. Pack, *Phys. Rev. B*, 1976, **13**, 5188-5192.
33. M. Methfessel and A. T. Paxton, *Phys. Rev. B*, 1989, **40**, 3616-3621.
34. D. Kong, H. Wang, J. J. Cha, M. Pasta, K. J. Koski, J. Yao and Y. Cui, *Nano Lett.*, 2013, **13**, 1341-1347.
35. D. Y. Chung, S. K. Park, Y. H. Chung, S. H. Yu, D. H. Lim, N. Jung, H. C. Ham, H. Y. Park, Y. Piao, S. J. Yoo and Y. E. Sung, *Nanoscale*, 2014, **6**, 2131-2136.
36. J. Xie, J Zhang, S. Li, F. Grote, X. Zhang, H. Zhang. R. Wang, Y. Lei, B. Pan and Y. Xie, *J. Am. Chem. Soc.*, 2013, **135**, 17881-17888.
37. K. Xu, F. Wang, Z. Wang, X. Zhan, Q. Wang, Z. Cheng, M. Safdar and J. He, *ACS Nano*, 2014, **8**, 8468-8476.
38. H. Wang, Z. Lu, D. Kong, J. Sun, T. M. Hymel and Y. Cui, *ACS Nano*, 2014, **8**, 4940-4947.
39. W. Zhang, Y. Wang, Z. Wang, Z. Zhong and R. Xu, *Chem. Commun.*, 2010, **46**, 7631-7633.
40. T. Bligaard, J. K. Nørskov, S. Dahl, J. Matthiesen, C. H. Christensen and J. Sehested, *J. Catal.*, 2004, **224**, 206-217
41. S. A. Vilekar, I. Fishtik and R. Datta, *J. Electrochem. Soc.*, 2010, **157**, B1040-B1050.
42. E. Skúlason, V. Tripkovic, M. E. Björketun, S. Gudmundsdóttir, G. Karlberg, J. Rossmeisl, T. Bligaard, H. Jónsson and J. K. Nørskov, *J. Phys. Chem. C*, 2010, **114**, 18182-18197.
43. M. Gong, W. Zhou, M. C. Tsai, J. Zhou, M. Guan, M. C. Lin, B. Zhang, Y. Hu, D. Y. Wang, J. Yang, S. J. Pennycook, B. J. Hwang and H. Dai, *Nat. Commun.*, 2014, **5**. 4695-4700
44. H. Wang, D. Kong, P. Johanes, J. J. Cha, G. Zheng, K. Yan, N. Liu and Y. Cui, *Nano Lett.*, 2013, **13**, 3426-3433.
45. C.-B. Ma, X. Qi, B. Chen, S. Bao, Z. Yin, X. -J. Wu, Z. Luo, J. Wei, H. -L. Zhang and H. Zhang, *Nascale*, 2014, 6, 5624-5629.

46. C. Tsai, F.A-.Pedersen and J. K. Norskov, *Nano Lett*, 2014, **14**, 1381-1387.